

# The GREGOR Fabry-Pérot Interferometer and its companion the Blue Imaging Solar Spectrometer

**Klaus G. Puschmann**

**Carsten Denker**

**Horst Balthasar**

**Rohan E. Louis**

**Emil Popow**

**Manfred Woche**

Leibniz-Institut für Astrophysik Potsdam

14482 Potsdam

Germany

E-mail: [kgp@aip.de](mailto:kgp@aip.de)

**Christian Beck**

Instituto de Astrofísica de Canarias

38205 La Laguna, Tenerife

Spain

**Thomas Seelemann**

LaVision

37081 Göttingen

Germany

**Reiner Volkmer**

Kiepenheuer-Institut für Sonnenphysik

79104 Freiburg

Germany

**Abstract.** The GREGOR Fabry-Pérot Interferometer (GFPI) is one of three first-light instruments of the German 1.5-meter GREGOR solar telescope at the Observatorio del Teide, Tenerife, Spain. The GFPI allows fast narrow-band imaging and post-factum image restoration. The retrieved physical parameters will be a fundamental building block for understanding the dynamic Sun and its magnetic field at spatial scales down to  $\sim 50$  km on the solar surface. The GFPI is a tunable dual-etalon system in a collimated mounting. It is designed for spectrometric and spectropolarimetric observations between 530–860 nm and 580–660 nm, respectively, and possesses a theoretical spectral resolution of  $\mathcal{R} \approx 250,000$ . Large-format, high-cadence CCD detectors with sophisticated computer hard- and software enable the scanning of spectral lines in time-spans equivalent to the evolution time of solar features. The field-of-view (FOV) of  $50'' \times 38''$  covers a significant fraction of the typical area of active regions in the spectroscopic mode. In case of Stokes-vector spectropolarimetry, the FOV reduces to  $25'' \times 38''$ . We present the main characteristics of the GFPI including advanced and automated calibration and observing procedures. We discuss improvements in the optical design of the instrument and show first observational results. Finally, we lay out first concrete ideas for the integration of a second FPI, the Blue Imaging Solar Spectrometer (BLISS), which will explore the blue spectral region below 530 nm. © 2018 Society of Photo-Optical Instrumentation Engineers

Paper 121432SSPR compiled June 5, 2018.

## 1 Introduction

Solar physics has made tremendous progress during recent years thanks to numerical simulations and high-resolution spectropolarimetric observations with modern solar telescopes such as the Swedish Solar Telescope,<sup>1</sup> the Solar Optical Telescope on board the Japanese HINODE satellite,<sup>2</sup> and the stratospheric Sunrise telescope.<sup>3</sup> Taking the nature of sunspots as an example, many important new observational results have been found, e.g., details about the brightness of penumbral filaments, the Evershed flow, the dark-cored penumbral filaments, the net circular polarization, and the moving magnetic features in the sunspot moat. Telescopes with apertures of about 1.5 m such as the GREGOR solar telescope<sup>4,5</sup> or the New Solar Telescope<sup>6,7</sup> will help to discriminate among competing sunspot models and to explain the energy balance of sunspots. New results on the emergence, evolution, and disappearance of magnetic flux at smallest scales can also be expected. However, these 1.5-meter telescopes are just the precursors of the next-generation solar telescopes, i.e., the Advanced Technology Solar Telescope<sup>8</sup> and the European Solar Telescope,<sup>9</sup> which will finally be able to resolve the fundamental scales of the solar photosphere, namely, the photon mean free path and the pressure scale height.

Fabry-Pérot interferometers (FPIs) have gained importance in solar physics during the last decades because they deliver high spatial and spectral resolution. A growing number of such instruments is in operation at various telescopes.

Although most of these instruments have been initially designed only for spectroscopy, most of them have now been upgraded to provide full-Stokes polarimetry.<sup>10,11,12</sup> The Universitäts-Sternwarte Göttingen developed an imaging spectrometer for the German Vacuum Tower Telescope (VTT) in the early 1990s.<sup>13</sup>

A fundamental renewal of the Göttingen FPI during the first half of 2005 was the starting point of the development of a new FPI for the 1.5-meter GREGOR telescope.<sup>14</sup> New narrow-band etalons and new large-format, high-cadence CCD detectors were integrated into the instrument, accompanied by powerful computer hard- and software. From 2006 to 2007, the optical design for the GREGOR Fabry-Pérot Interferometer (GFPI) was developed, the necessary optical elements were purchased, and the opto-mechanical mounts were manufactured.<sup>15</sup> An upgrade to full-Stokes spectropolarimetry followed in 2008.<sup>16,17</sup> In 2009, the Leibniz-Institut für Astrophysik Potsdam took over the scientific responsibility for the GFPI, and the instrument was finally installed at the GREGOR telescope.<sup>19</sup> During the commissioning phase in 2011, the software was prepared for TCP/IP communication with external devices according to the Device Communication Protocol (DCP<sup>20</sup>) and three computer-controlled translation stages (two filter sliders and one mirror stage) were integrated into the GFPI.<sup>21</sup> This permits automated observing and calibration procedures and facilitates easy operations during observing runs. The present article is a modified version of a contribution<sup>22</sup> to the SPIE confer-

ence ‘Ground-Based and Airborne Instrumentation for Astronomy IV’, which took place in Amsterdam in June 2012. A complementary description of the GFPI<sup>23</sup> has been published in the meanwhile in a special issue of *Astronomische Nachrichten/AN* (Volume 333, Issue 9) dedicated to the GREGOR solar telescope.

## 2 GREGOR solar telescope

The 1.5-meter GREGOR telescope is the largest European solar telescope and is designed for high-precision measurements of dynamic photospheric and chromospheric structures and their magnetic field. Some key scientific topics of the GREGOR telescope are: the interaction between convection and magnetic fields in the photosphere, and the enigmatic heating mechanism of the chromosphere. The inclusion of a spectrograph for stellar activity studies and the search for solar twins expand the scientific usage of the GREGOR telescope to the nighttime domain.<sup>24</sup>

The GREGOR telescope replaced the 45-cm Gregory-Coudé Telescope, which had been operated on Tenerife since 1985. The construction of the new telescope was carried out by a consortium of several German institutes, namely, the Kiepenheuer-Institut für Sonnenphysik Freiburg, the Leibniz-Institut für Astrophysik Potsdam (AIP), and the Institut für Astrophysik Göttingen. In 2009, the Max-Planck-Institut für Sonnensystemforschung in Katlenburg-Lindau took over the contingent of the latter institute. The consortium maintains partnerships with the Instituto de Astrofísica de Canarias in Spain and the Astronomical Institute of the Academy of Sciences of the Czech Republic in Ondřejov.

The GREGOR telescope is an alt-azimuthally mounted telescope with an open structure and an actively cooled light-weighted Zerodur primary mirror. The completely retractable dome<sup>25</sup> enables wind flushing through the telescope to facilitate cooling of telescope structure and optics.<sup>26,27</sup> The water-cooled field stop at the primary focus provides a field-of-view (FOV) with a diameter of 150". The light is reflected via two elliptical mirrors and several flat mirrors into the optical laboratory. Passing the GREGOR adaptive optics system (GAOS),<sup>28</sup> the light is finally distributed to the scientific instruments. The removable GREGOR Polarimetric Unit (GPU),<sup>29</sup> which was developed at the AIP, is located near the secondary focus and ensures high-precision polarimetric calibration. In addition, a telescope polarization model has been developed,<sup>18</sup> since the instrumental polarization is time-dependent due to the alt-azimuthal mount. Three first-light instruments have been commissioned in 2011 and passed through science verification in 2012: the GRating Infrared Spectrograph (GRIS),<sup>30</sup> the Broad-Band Imager (BBI),<sup>31</sup> and the GFPI.<sup>23</sup> GRIS and GFPI can be used simultaneously. A dichroic beamsplitter directs wavelengths above 650 nm to the spectrograph, whereas all shorter wavelengths are reflected towards the GFPI. In the near future, this beamsplitter can be exchanged with a different one with a cutoff above 860 nm.

## 3 GREGOR Fabry-Perot Interferometer

### 3.1 Optical design

The GFPI is mounted on five optical tables and is protected by an aluminum housing to prevent pollution of the optics

by dust and to reduce stray-light. The optical layout of the instrument is shown in Fig. 1. Behind the science focus F4, four achromatic lenses TL1, TL2, HL1, & HL2 create two more foci F5 & F6 and two pupil images P1 & P2 in the narrow-band channel NBC. The etalons FPI1 & FPI2 are placed in the vicinity of the secondary pupil in the collimated light beam. A neutral density filter NDF between the two etalons with a transmission of 63% reduces the inter-etalon reflexes. The beam in the NBC is folded twice by M2 & M5 at a distance of 500 mm and 400 mm from F5 and HL2, respectively, to minimize the instrument envelope. Two field stops FS1 & FS2 prevent an over-illumination of the detectors, where the secondary adjustable field stop especially avoids an overlap of the two images created by the removable dual-beam full-Stokes polarimeter. A beamsplitter cube BS2 near F5 directs 5% of the light to the broad-band channel BBC. There, the two achromatic lenses TL3 & TL4 are chosen such that the image scale of the detectors CCD1 & CCD2 is exactly the same. The simultaneous recording of broad- and narrow-band images is a prerequisite for post-factum image reconstruction. Several image reconstruction techniques are already implemented in a data pipeline presently being developed at the AIP.<sup>22</sup> A detailed description of these techniques and a comparison of related results has been recently published.<sup>10</sup> A dichroic beamsplitter BS1 just behind the science focus F4 sends the blue part of the spectrum (below 530 nm) to the Blue Imaging Channel BIC. One-to-one imaging with the lenses TL1a & TL2a provides the option of recording broad-band images in the wavelength range 380–530 nm with two pco.4000 cameras CCD1a & CCD2a behind beamsplitter BS2a in parallel to NBC and BBC or GRIS observations. This imaging channel will be replaced in the future by the Blue Imaging Solar Spectrometer (BLISS), which is described in Section 5.

Three computer-controlled precision translation stages facilitate automated observing sequences. The two stages FSL1 & FSL2 are used to switch between two sets of interference filters. The filters restrict the bandpass of BBC and NBC to a full-width at half-maximum (FWHM) of 10 nm and 0.3–0.8 nm, respectively. The near-focus position of the sliders excluded the usage of a filterwheel because of the required positioning accuracy in the order of micrometers. Only two different interference filters can be mounted on each slider because of the limited space on the optical tables. The pre-filters of each channel can be tilted to optimize the wavelength of the transmission maximum. At present, the optical elements of the GFPI are not super-achromatic. Thus, a chromatic focus shift restricts the maximum spectral distance between two different pre-filters/spectral lines to about 100 nm.<sup>23</sup> A third stage inserts a deflection mirror M1 into the light path to take calibration data with a continuum-light source for spectral calibration purposes (white-light channel). A laser/photo-multiplier channel for finesse adjustment of the etalons completes the optical setup.

### 3.2 Cameras, etalons, and control software

The GFPI data acquisition system consists of two Imager QE CCD cameras with Sony ICX285AL detectors, which have a full-well capacity of 18,000 e<sup>-</sup> and a read-out noise of 4.5 e<sup>-</sup>. The detectors have a spectral response from 320–900 nm with a maximum quantum efficiency of ~60% at

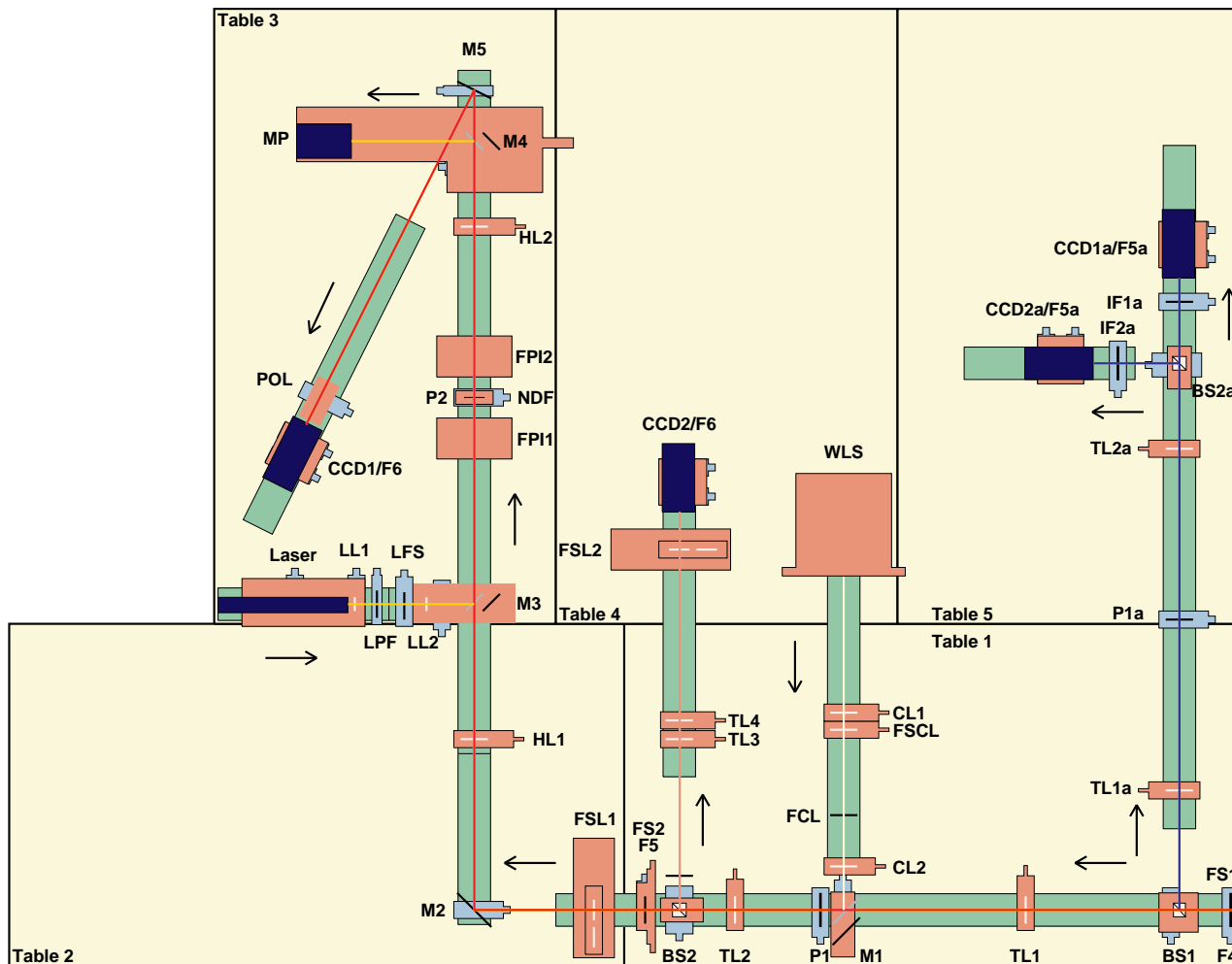


**Fig. 1** Up-to-scale drawing of the GFPI, including narrow-band channel (NBC, marked as red beam), broad-band channel (BBC, salmon beam), blue imaging channel (BIC, blue beam), and all auxiliary channels, i.e., white-light channel (off-wight beam) and laser/photo-multiplier channel (yellow beam). The light from the telescope enters the instrument at the science focus F4. Black arrows denote the light direction in the individual channels. The optical elements of BIC are labeled with an extra "a". CCD1, CCD2: Imager QE detectors; CCD1a, CCD2a: pco.4000 detectors; FPI1, FPI2: narrow-band etalons; NDF: neutral density filter; TL1 ( $f = 600$  mm,  $d = 63$  mm), TL2 ( $f = 250$  mm,  $d = 40$  mm), TL1a ( $f = 500$  mm,  $d = 63$  mm), TL2a ( $f = 500$  mm,  $d = 80$  mm), TL3 ( $f = 400$  mm,  $d = 63$  mm), TL4 ( $f = 600$  mm,  $d = 63$  mm), HL1 ( $f = 1000$  mm,  $d = 80$  mm), HL2 ( $f = 1500$  mm,  $d = 100$  mm); achromatic lenses; CL1 ( $f = 300$  mm,  $d = 63$  mm), CL2 ( $f = 150$  mm,  $d = 40$  mm); plano-convex lenses; M1, M3, M4: removable folding mirrors; M2, M5: fixed folding mirrors (60 mm  $\times$  85 mm); F4, F5, F6, F5a, FCL: foci; P1, P1a, P2: pupil sliders; BS1, BS2, BS2a: beam splitters (40 mm  $\times$  40 mm); FS1, FS2, FSCL: field stops; WLS: white-light source (slide projector); FSL1, FSL2: filter sliders; IF1a, IF2a: interference filters; POL: full-Stokes polarimeter; LL1, LL2: laser lenses; LPF: laser polarization filter; LFS: laser field stop; and MP: photomultiplier.

550 nm. The chips have  $1376 \times 1040$  pixels with a size of  $6.45 \mu\text{m} \times 6.45 \mu\text{m}$ . The image scale at both cameras is  $0.0361'' \text{ pixel}^{-1}$ , which leads to a FOV of  $50'' \times 38''$  in the spectroscopic mode. Due to the dual-beam configuration, the FOV shrinks to  $25'' \times 38''$  when using the polarimetric mode of the instrument. The maximal blueshift due to the collimated mounting of the etalons is about 4.3 pm at 630 nm. The cameras are triggered by analog TTL signals of a programmable timing unit (PTU). The analog-digital conversion of the CCD-images is carried out with 12-bit resolution. The data recorded by the cameras are passed via digital coaxial cables to the GFPI control computer and are stored on a RAID 0 system.<sup>21</sup>

Two pco.4000 cameras in stock at the observatory can

be used for imaging in the BIC. The pco.4000 camera has a full-well capacity of  $60,000 e^-$  and a read-out noise of  $11 e^-$ . The detector has a spectral response from 320–900 nm with a quantum efficiency of  $\sim 32\%$  ( $\sim 45\%$ ) at 380 (530) nm. The chip has  $4008 \times 2672$  pixels, each with a size of  $9 \mu\text{m} \times 9 \mu\text{m}$ . The image scale at both cameras is  $0.031'' \text{ pixel}^{-1}$ . Because of a vignetting of the beam by BS1 and BS2a only  $2000 \times 2672$  pixels can be used resulting in a FOV of  $63'' \times 84''$ . Three interference filters for Ca II H  $\lambda 396.8$  nm, Fraunhofer G-band  $\lambda 430.7$  nm, and blue continuum  $\lambda 450.6$  nm are available, which have a FWHM = 1 nm and a transmission better than 60%.

The two GFPI etalons manufactured by IC Optical Systems (ICOS) have a diameter  $\varnothing = 70$  mm, a measured fi-

Tab. 1 Summary of the GFPI observations.

Channel	$\lambda_0$ [nm]	$\Delta t$ [ms]	$I$ [counts]	PHA (F4)	PH (F3)	PH (F2)	TG	QS	SP	PF
NBC ( $1 \times 1$ binning)	543.3	40	2400	x	x	—	x	x	x	x
BBC ( $1 \times 1$ binning)	543.3	40	—	x	x	—	x	x	x	—
NBC ( $2 \times 2$ binning)	543.3	30	3500	—	—	—	x	x	—	x
NBC ( $2 \times 2$ binning)	557.6	40	2100	—	x	—	x	x	—	x
NBC ( $2 \times 2$ binning)	617.3	10	3200	—	x	—	x	x	—	x
Ca II H	396.8	15	9230	x	x	x	x	x	x	—
G-band	430.7	6	10350	x	x	x	x	x	x	—
Blue continuum	450.6	3	11300	x	x	x	x	x	x	—

Note. — Central wavelength  $\lambda_0$ , exposure time  $\Delta t$ , and mean intensity  $I$  for all observations (PHA: pinhole array, PH: pinhole, TG: target, QS: quiet Sun, SP: sunspot, and PF: pre-filter).

ness  $\mathcal{F} \sim 46$ , spacings  $d = 1.1$  and  $1.4$  mm, and a high-reflectivity coating ( $R \sim 95\%$ ) in the wavelength range from 530–860 nm. The resulting FWHM of the instrument is on the order of 1.9–5.6 pm and leads to a theoretical spectral resolution of  $\mathcal{R} \sim 250,000$ . However, the etalon spacings are not optimal because of historical reasons, thus off-band contributions can become critical when using too broad pre-filters.<sup>23</sup> All etalons are operated by three-channel CS100 controllers manufactured by ICOS. The cavity spacings are digitally controlled by the GFPI control computer via RS-232 communication. A thermally insulated box protects pupil and etalons from stray-light and air flows inside the instrument.

The communication between internal (cameras, etalons, and filter and mirror sliders) and peripheral devices (telescope, AO system, AO filter wheel, GPU, GRIS, etc.) is controlled by the software package DaVis from LaVision in Göttingen, which has been adapted to the needs of the spectrometer.<sup>14,21</sup> The modification of the software for TCP/IP communication with external devices using DCP allows an easy implementation of automated observing procedures.<sup>21</sup> All observing modes such as etalon adjustment, line finding, flat-fielding, recording of dark, pinhole, and target images, continuum scans, and recording of scientific data are now automated.

### 3.3 Polarimetry with the GFPI

The science verification time in 2012 was mostly devoted to spectroscopy. Nevertheless, the GFPI is equipped with a dual-beam full-Stokes polarimeter<sup>16,23</sup> that can be inserted in front of the detector in the NBC. The polarimeter consists of two ferro-electric liquid crystal retarders (FLCRs) and a modified Savart-plate. The first liquid crystal acts as a half-wave plate and the second one as a quarter-wave plate at a nominal wavelength of 630 nm. The modified Savart-plate consists of two polarizing beamsplitters and an additional half-wave plate, which exchanges the ordinary and the extraordinary beam. With this configuration, the separation of the two beams is optimized and the orientation of the astigmatism in both beams is the same so that it can be corrected by a cylindrical lens. For the present set of FLCRs their properties (retardation and fast axis orientation) have been measured so far only for the spectral range 580–660 nm.<sup>23</sup> An au-

tomated polarimetric calibration procedure will be integrated during an upcoming technical campaign in April 2013. At that time the GREGOR polarimetric calibration unit will be available for the visible-light range. This will be the starting point for polarimetry with the GFPI at the GREGOR solar telescope. A future enlargement of the reduced FOV in the polarimetric dual-beam mode would be possible by replacing the Imager QE cameras with modern and large-format sCMOS cameras, which have also much higher frame rates (cf. Sect. 5). However, this would require an additional redesign of the polarimeter, because presently the FOV is also limited by the size of the calcites of the polarimeter.

## 4 GFPI science verification

We took several data sets in a technical campaign from 15 May to 1 June 2012 for a first characterization of the GFPI performance. The AO system was not available because of technical problems with the control computer. Thus, our efforts have been restricted to an optimization of the system and to observations of test data as measures for intensity levels, image quality, spectral resolution, stray-light, and other performance indicators of NBC, BBC, and BIC. Several problems related to the RS-232 communication with the FPI controllers were resolved so that a stable finesse is now achieved over several days. In addition, the timing between cameras and etalons has been optimized to ensure that images are only taken when the etalon spacing has settled to its nominal value.

### 4.1 Imaging spectrometric data

Three complete data sets with  $2 \times 2$  binning ( $\sim 0.072''$  pixel<sup>-1</sup>) were taken on 31 May and 1 June 2012, which included images of the target TG and pinhole PH mounted in the AO filter wheel at F3 (telescope focal plane). The observations covered neutral iron lines at 543.4 nm, 557.6 nm, and 617.3 nm. The Fe I  $\lambda 543.4$  nm line had already been scanned on 27 May at full spatial resolution ( $0.036''$  pixel<sup>-1</sup>) including images of a pinhole array in F4 (science focus at the entrance of the GFPI). Simultaneous BBC images were recorded (Tab. 1). Line scans with the GFPI were usually carried out using a step width of eight digital-analog (DA) steps, whereas the pre-filter scans were performed with one DA step. One DA step corresponds to 0.26–0.41 pm in the



Tab. 2 NBC pre-filter characteristics.

Filter	$\lambda_0$ [nm]	FWHM [nm]	$T$ [%]	Binning	$\Delta t$ [ms]	$I$ [counts]	Frame rate [Hz]
ANDV11436	543.4	0.4	38	- / - / 2 × 2	60 / 100 / 30	1200 / 2000 / 3500	7 / 5 / 11
1100 BARR9	543.4	0.6	70	-	40 / 60	1700 / 2700	7 / 6
ANDV5288	557.6	0.3	40	2 × 2	40	2100	11
DV5289 AM-32389	569.1	0.3	45	-	60 / 100	1200 / 2000	6 / 5
ANDV9330	617.3	0.7	80	- / - / 2 × 2	20 / 60 / 80	1200 / 3400 / 3200	9 / 6 / 16

Note. — Continuum intensities  $I$  at wavelengths  $\lambda_0$  for filters with peak transmissions  $T$  and exposure times  $\Delta t$ .

spectral range from 530–860 nm.

Broad-band data were taken in the BIC on 26 and 27 May 2012 just before the NBC and BBC measurements. The observing scheme was the same for all available pre-filters (396.8 nm, 430.7 nm, 450.6 nm). In addition to a few observations of the quiet Sun and a sunspot, images of the target and pinhole in F3, the pinhole-array in F4, and the pinhole mounted in the GPU at F2 are also included. All data in the BIC were taken with a combination of two spare lenses with  $f = 500$  mm and 1250 mm because a second lens with  $f = 500$  mm was not available yet. Thus, the image scale of  $0.0124'' \text{ pixel}^{-1}$  oversamples the diffraction limit at these wavelengths by a factor of about three. The proper image scale of  $0.032'' \text{ pixel}^{-1}$  has been obtained in a following campaign by an one-to-one imaging.

#### 4.2 Intensity estimates for the narrow-band channel

The wavelength  $\lambda_0$ , FWHM, and transmission  $T$  of different NBC filters are summarized in Tab. 2 together with the selected binning, the counts at continuum wavelengths, and frame rates at a given exposure time  $\Delta T$ . The results reveal that at full spatial resolution very long exposure times of up to 100 ms are necessary to achieve at least 2000 counts in the continuum of most of the measured spectral lines for most of the filters with  $T \sim 40\%$  and a FWHM  $\sim 0.3\text{--}0.4$  nm. As a consequence, one can reach only very low frame rates. A  $2 \times 2$ -pixel binning speeds up the observations and reduces the exposure times. The situation changes when choosing filters with higher transmission. The 617.3 nm filter with  $T \sim 80\%$  and a FWHM  $\sim 0.74$  nm yields reasonable frame rates and exposure times even without binning.

#### 4.3 Estimates of the spatial point spread function

Knowledge of the instrumental point spread function (PSF) provides an estimate of both the spatial resolution and the spatial stray-light level.<sup>32,33</sup> Using a reference such as a pinhole or a blocking edge in the focal plane, the PSF of all optics downstream can be derived. The combined PSF of time-variable seeing, telescope, and post-focus instruments, can also be derived from the observations of, e.g., sunspots with their steep spatial intensity gradients.

The PSF of the optical train at the GREGOR telescope relevant for the different GFPI channels was calculated based on reduced images of pinholes located in the focal planes F4, F3, F2, and on sunspot images (see Tab. 1). All available calibration images, e.g., target or pinhole images, were averaged for each wavelength step or image burst. However, only a single image was selected for solar observations because of

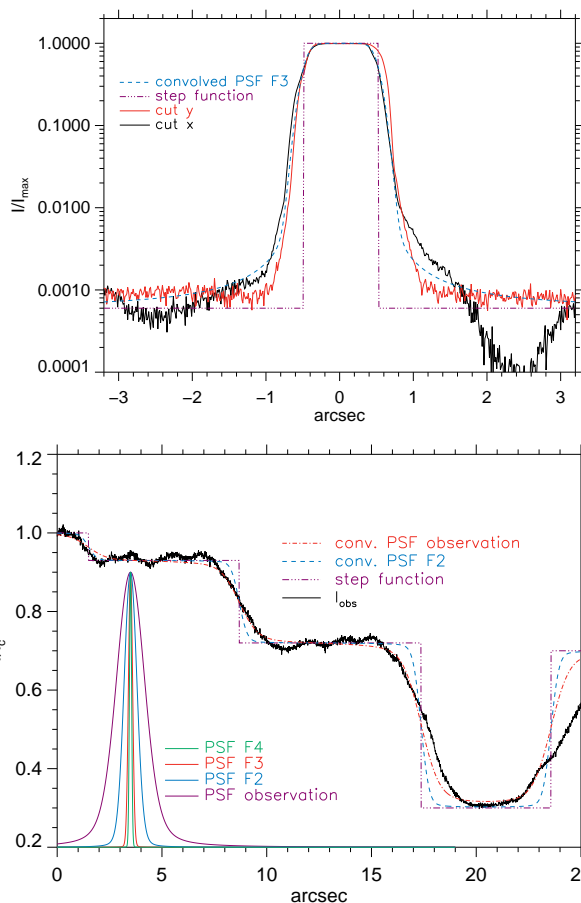
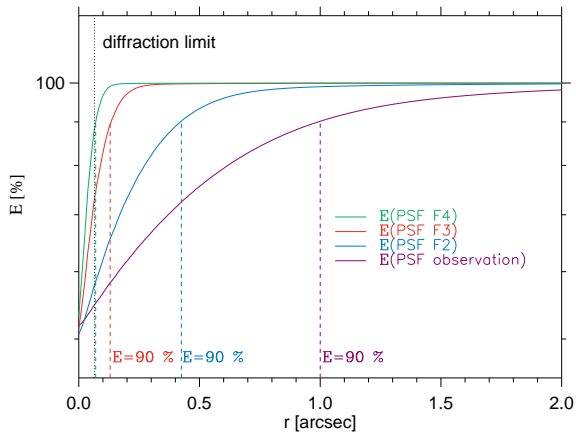


Fig. 2 Derivation of the PSF estimate at 430 nm for the pinhole in F3 (top) and for the complete optical train from a sunspot observation (bottom), where the PSF estimates of the four different focal planes are displayed in the lower left corner.

the variable seeing. The pinhole images were normalized to the maximum intensity  $I_{\max}$  inside the FOV, whereas the sunspot data were normalized to unity in a quiet Sun region. All data were taken without real-time correction of the AO system and consequently correspond to the static performance of the optical system.

#### 4.4 Derivation of the point spread function estimates

To obtain an estimate of the PSF, we took cuts along the  $x$ - and  $y$ -axes of the CCD across the center of the pinhole in each pinhole observation. We defined a step function that is



**Fig. 3** Energy enclosed within the radius  $r$  for the PSF estimates at 430.7 nm of the four different focal planes. The *dashed vertical lines* denote the radius where 90% of the energy is enclosed. The *dotted vertical line* denotes the diffraction limit at 430.7 nm.

assumed to represent the physical extent of the true pinhole. The borders of the step function were set to intersect the observed intensity along the cuts at about the 50% level (top panel of Fig. 2). We constructed a convolution kernel from a combination of a Gaussian (variance  $\sigma$ ) and a Lorentzian function (parameter  $a$ ) and convolved the step function with the kernel. A modification of the parameters ( $\sigma$ ,  $a$ ) within a specific range yielded finally the kernel that best matched the convolved step function and the observed intensity along the horizontal and vertical cuts. The same method was applied to all pinhole observations (F4, F3, and F2) to derive a PSF estimate for each focal plane and wavelength. The sunspot observations were modeled by a similar step function at the two transitions between quiet Sun, penumbra, and umbra (bottom panel of Fig. 2).

The resulting PSF estimates of the four focal planes for the BIC data at 430.7 nm are displayed in the lower left corner of the bottom panel of Fig. 2. The width of the PSF estimates is similar for F4 and F3, where only static optical components contribute to the PSF, but increases significantly when passing to the focal plane F2 that experiences telescope seeing and seeing fluctuations along the Coudé train. The PSF derived from the sunspot observations includes all seeing effects and roughly doubles its width relative to the PSF at F2.

PSF estimates for all four focal planes were obtained in case of the BIC data at 430.7 nm, but only for some of the focal planes in case of the BBC and NBC data (see Tab. 3). The optical performance and the expected stray-light level can be best quantified from the total energy enclosed in a given radius, i.e., a radial integration of the PSF. Figure 3 shows the enclosed energy  $E$  for the PSF estimates at 430.7 nm. The curves provide two characteristic values, namely, the energy enclosed at the diffraction limit  $E(r_{DL})$  and the radius  $r(E = 90\%)$  at which 90% of the energy is enclosed. The former value gives an estimate of the generic stray-light when subtracted from 100%. The latter value can be used as generic estimate of the spatial resolution. Table 3 lists the two values for all analyzed wavelengths and channels, i.e., BIC, BBC and NBC at specific wavelengths.

A comparison between the value of the diffraction limit

Channel	BIC $\lambda 430.7$ nm				BBC $\lambda 543.4$ nm		
Sampling	0.0124'' pixel <sup>-1</sup> (0.0126'' pixel <sup>-1</sup> )				0.034'' pixel <sup>-1</sup> (0.036'' pixel <sup>-1</sup> )		
Diff. limit	0.072''				0.091''		
Focal plane	F4	F3	F2	Solar obs.	F4	F3	Solar obs.
$r(E = 90\%)$ [']	0.07	0.13	0.43	1.00	0.11	0.17	2.4
$E(r_{DL})$	90%	73%	58%	55%	85%	74%	52%

Channel	NBC $\lambda 543.4$ nm			NBC $\lambda 557.6$ nm		NBC $\lambda 617.3$ nm	
Sampling	0.034'' pixel <sup>-1</sup> (0.036'' pixel <sup>-1</sup> )			0.069'' pixel <sup>-1</sup> (0.072'' pixel <sup>-1</sup> )		0.067'' pixel <sup>-1</sup> (0.072'' pixel <sup>-1</sup> )	
Diff. limit	0.091''			0.094''		0.103''	
Focal plane	F4	F3	Solar obs.	F3	F3	F3	
$r(E = 90\%)$ [']	0.12	0.20	2.65	0.19	0.19	0.19	
$E(r_{DL})$	85%	71%	51%	75%	76%	76%	

**Tab. 3** Summary of observations at different wavelengths. Theoretical values are given in parentheses.

and the radius where 90% of the energy is enclosed shows that the optics behind F4 performs close to the diffraction limit. The optics downstream of F3 performs slightly worse with a total enclosed energy of about 70–75% of the diffraction-limited case. This implies a spatial stray-light level of about 25% created by the optics downstream of F3. The corresponding value at F4 is about 10–15%. The values of both the stray-light level and  $r(E = 90\%)$  experience a profound jump when passing to F2 and beyond. However we note, that all these data were taken at mediocre seeing conditions and without AO correction.

#### 4.5 Spectral resolution, spectral stray-light, and blue-shift

The spectral resolution and the *spectral* stray-light inside the NBC was estimated by a convolution of Fourier Transform Spectrograph (FTS) atlas spectra<sup>34,35</sup> with a Gaussian of width  $\sigma$  and a subsequent addition of a constant wavelength-independent stray-light offset  $\beta$ .<sup>36,37</sup> This component of stray-light corresponds to light scattered onto the CCD detector without being spectrally resolved. Therefore, it changes the line depth of observed spectral lines. The convolved FTS spectra in each wavelength range were compared with sets of spatially averaged observational profiles that either covered the full pre-filter transmission curve or only the line inside the same range that is usually recorded in science observations (543.4 nm, 557.6 nm, 617.3 nm). The upper panel of Fig. 4 shows the average observed spectrum at Fe I  $\lambda 617.3$  nm, the original FTS spectrum, and the FTS spectrum after the convolution with the best-fit Gaussian kernel and the addition of the stray-light offset. The method has some ambiguity between  $\sigma$  and  $\beta$ , which can be modified in opposite directions over some range near the best-fit values without significantly degrading the reproduction of the observed spectra. Therefore, the values listed in Tab. 4 have an error of about  $\pm 0.5$  pm in  $\sigma$  and  $\pm 5\%$  in  $\beta$ . The stray-light level  $\beta$  inside the NBC is below 10% and the spectral resolution is  $\mathcal{R} \sim 100,000$ , which is significantly below the theoretically expected value of  $\mathcal{R} \sim 250,000$ . The dispersion values derived from the observed spectra are listed in Tab. 4 and correspond to eight DA steps. In addition, we also con-

Tab. 4 Spectral characteristics of the GFPI data.

Wavelength	543.4 [nm]	557.6 [nm]	617.3 [nm]	630.25 <sup>10</sup>
Dispersion (8 DA) [pm]	2.08 (2.09)	2.15 (2.15)	2.36 (2.36)	2.31 (2.41)
Dispersion (1 DA) [pm]	— (0.261)	— (0.268)	— (0.296)	—
$\sigma$ [pm]	2.62	2.07	2.81	1.65
$\beta$ [%]	6.6	6.5	7.8	14
$\lambda/\sigma$ —	207200	269500	219700	381800
$\lambda/\Delta\lambda$ —	88200	114700	93500	162500
Max. blueshift [pm]	3.91 (3.72)	3.96 (3.82)	4.49 (4.23)	— (4.32)

Note. — Theoretical values are indicated in parentheses.

firmed the maximal blueshift induced in the spectra, which is caused by the etalon mounting inside a collimated beam. The blueshift was determined from a set of observational flat-field data. All resulting numbers for both dispersion and blueshift are close to the theoretically expected values (see Tab. 4).

Because of the surprisingly low spectral resolution, we spent substantial effort to clarify the source of this problem. We tried to match FTS spectra convolved with the Airy-function, resulting from a theoretical simulation based on a least-squares fit with the effective finesse and an additional parasitic light contribution as free parameters, with observed profiles from campaigns performed in July and August 2012. It turned out that a finesse of  $\sim 16$  instead of  $\sim 46$  and an additional parasitic light contribution of  $\sim 7\%$  are needed to fit the observed profile of, e.g., the 543.4 nm line (lower panel of Fig. 4).

A finesse of 16 is in clear contradiction to the results obtained from the finesse-adjustment by laser light that is performed every day at the beginning of each observational run. These adjustments revealed always a finesse of 40-50 for both etalons. Furthermore, a better spectral resolution using the same etalons was achieved at the VTT ( $\mathcal{R} \sim 160,000$ ).<sup>10</sup> Several possibilities which might explain these observations were explored, e.g., the variation of the finesse between the center and periphery of the etalon plates.<sup>38</sup> However, none of the additional tests were conclusive.

A precise re-alignment of the GFPI in 2013 will show, if a stricter requirement for the collimation of the beam through the etalons together with an adjustment of the parallelism of the etalons with a wider laser beam will result in a higher finesse. Additionally we will carry out tests in an optical laboratory to quantify cavity errors caused by, e.g., the micro-roughness of the etalon surfaces.<sup>39,40,41</sup>

#### 4.6 First observations supported by adaptive optics

First observations with the GFPI at GREGOR were obtained between 28 July and 7 August 2012 with real-time correction of wavefront deformations provided by GAOS. Several data sets covering different spectral lines (e.g., 543.4 nm, 617.3 nm, 630.2 nm), and different objects and disk positions have been reduced and analyzed during the last months.

Figure 5 and Movie 1 show a detailed example of two-

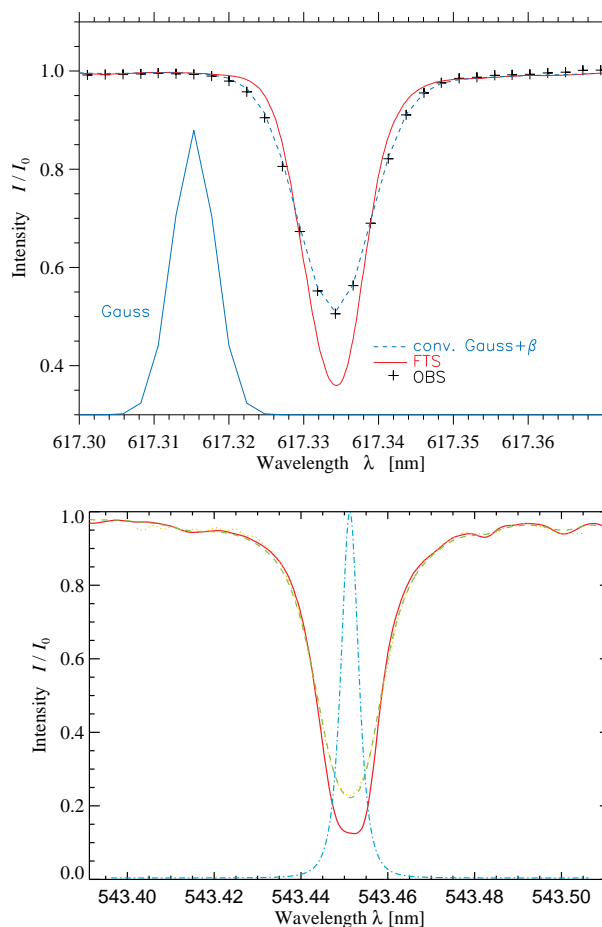
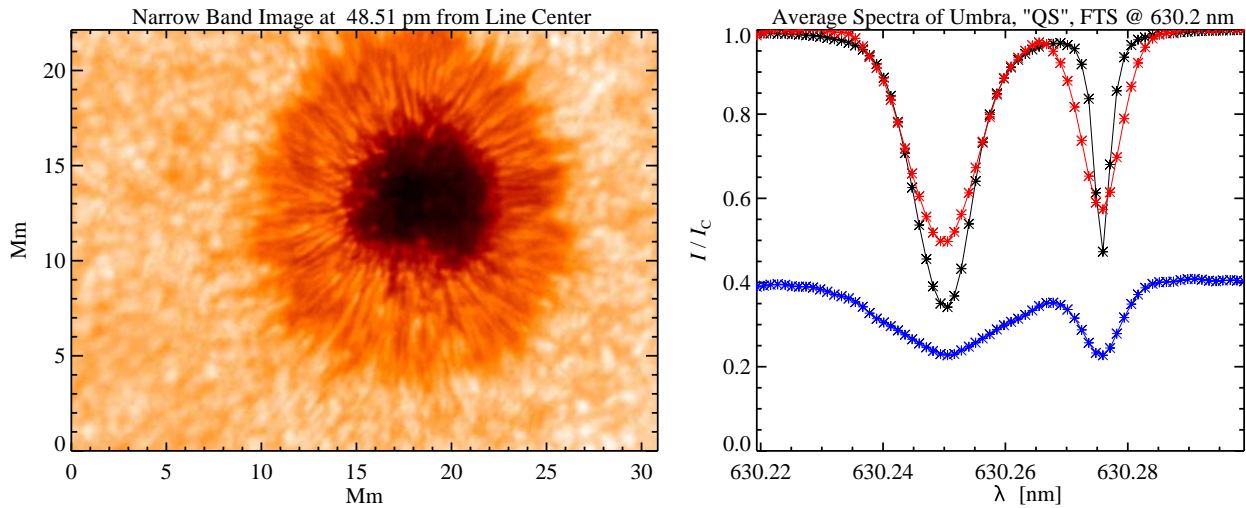


Fig. 4 Top: close-up of the Fe I  $\lambda 617.3$  nm line – observed spectrum (black pluses), FTS atlas spectrum (red solid line), and FTS convolved with the best-fit Gaussian kernel (blue dashed line). An appropriate stray-light offset ( $\beta$ ) was added after the convolution. The Gaussian kernel in the left corner is displayed in arbitrary units. Bottom: comparison of averaged observed quiet Sun spectrum (dotted orange line) of the Fe I  $\lambda 543.4$  nm line, FTS atlas spectrum (solid red line), and FTS-atlas spectrum convolved with an Airy-function (dash-dot turquoise line) obtained from a least-squares fit with the effective finesse and an additional parasitic light contribution as free parameters (dashed green line).

dimensional (2D) spectral line scans with the GFPI that were observed on 7 August 2012. The narrow-band continuum image around 630.2 nm is displayed in the left panel of Fig. 5. The spectral scan covered the Fe I  $\lambda 630.25$  nm line and the nearby telluric O<sub>2</sub> line with 70 steps in total and a step size of  $\Delta\lambda = 1.20$  pm (right panel of Fig. 5). Movie 1 shows all narrow-band images (left panel) at the consecutive spectral positions denoted by stars (right panel). The penumbral finestructure and individual umbral dots of the active region NOAA 11538 located at S22 W24 can be clearly identified in the spectral data. While throughout the solar line a significant change of structure and intensity contrast with height in the solar atmosphere is visible, the narrow-band images of the O<sub>2</sub> line just reflect the continuum intensity because of the telluric origin of the latter.

On 31 July, in total a 22-min time-series of the active region NOAA 11530 located at S24 W18 (heliocentric angle  $\theta = 30^\circ$ ) was obtained between 8:04 and 8:26 UT. Because



**Fig. 5** Left panel: Deconvolved continuum narrow-band image of the active region NOAA 11538 at 48.5 pm distance from the line center of the Fe I  $\lambda 630.25$  nm line. Right panel: measured average profiles of quiet sun (red), umbra (blue), and the FTS-atlas profile for comparison. The stars indicate the sampled spectral positions. [Movie 1](#) shows the entire line-scan, i.e., the deconvolved narrow-band images (left panel) at the consecutive spectral positions (right panel) in steps of 1.20 pm.

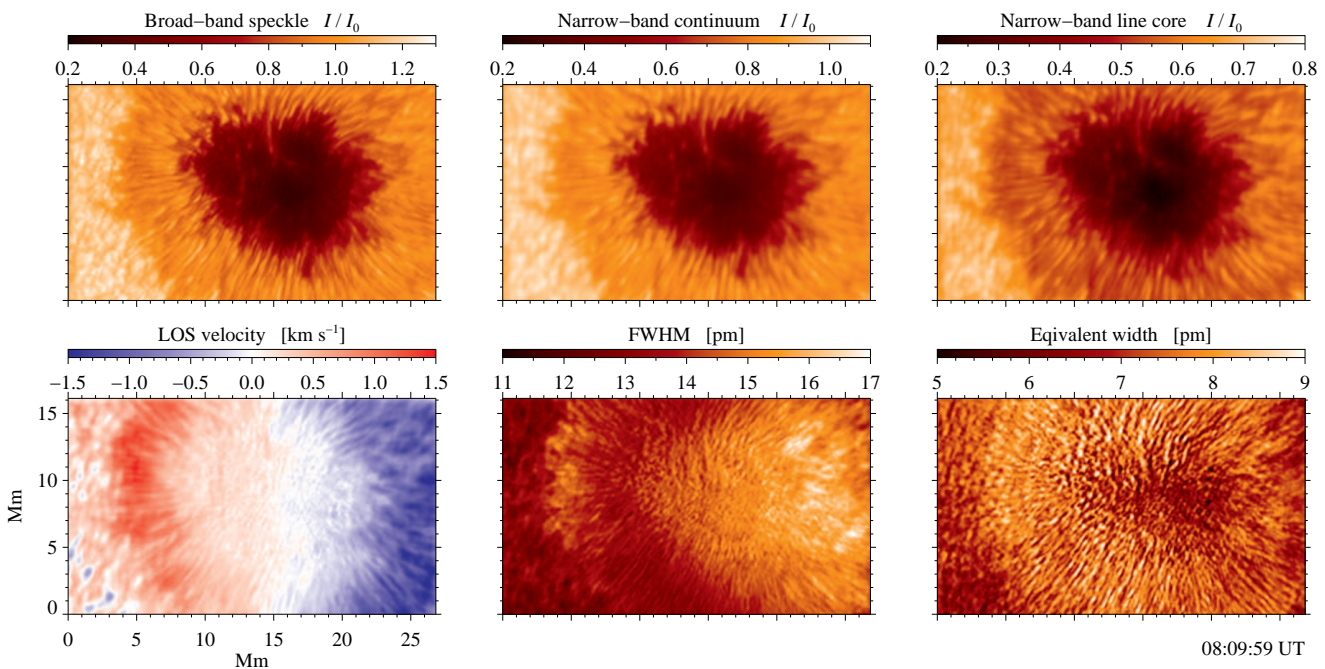


**Fig. 6** Snapshot of a 22-min time-series of the active region NOAA 11530. Upper panels: speckle-reconstructed broad-band image at 620 nm (left), speckle-deconvolved continuum narrow-band image (middle), and line-core narrow-band image (right) of the Fe I  $\lambda 617.3$  nm line. Bottom panels: line-core velocity (left), full-width at half-maximum (middle), and equivalent width (right). [Movie 2](#) shows the temporal evolution of the individual parameters.

the angle between solar south and the center of symmetry was  $33.8^\circ$ , the direction from center to limb corresponds to the  $x$ -axis of the displayed images. The spectral scan covered the Fe I  $\lambda 617.3$  nm line with 86 steps of  $\Delta\lambda = 1.17$  pm step size.

Figure 6 shows 2D maps of individual line parameters, i.e., normalized continuum intensity, line-core intensity, line-of-sight velocity, full-width at half-maximum, and equivalent width together with the speckle-reconstructed

broad-band image at 620 nm for one spectral scan. The temporal evolution of these line parameters over the entire time-series is presented in [Movie 2](#). In the LOS velocity map, the thinnest radial filamentary structures correspond to areas with almost zero velocity (spines), whereas the flow filaments on both center and limb sides are significantly wider (intraspines). Even with some fluctuations in the final image quality, the evolution of small-scale structures can be well followed, e.g., the inward motion of penumbral grains. The



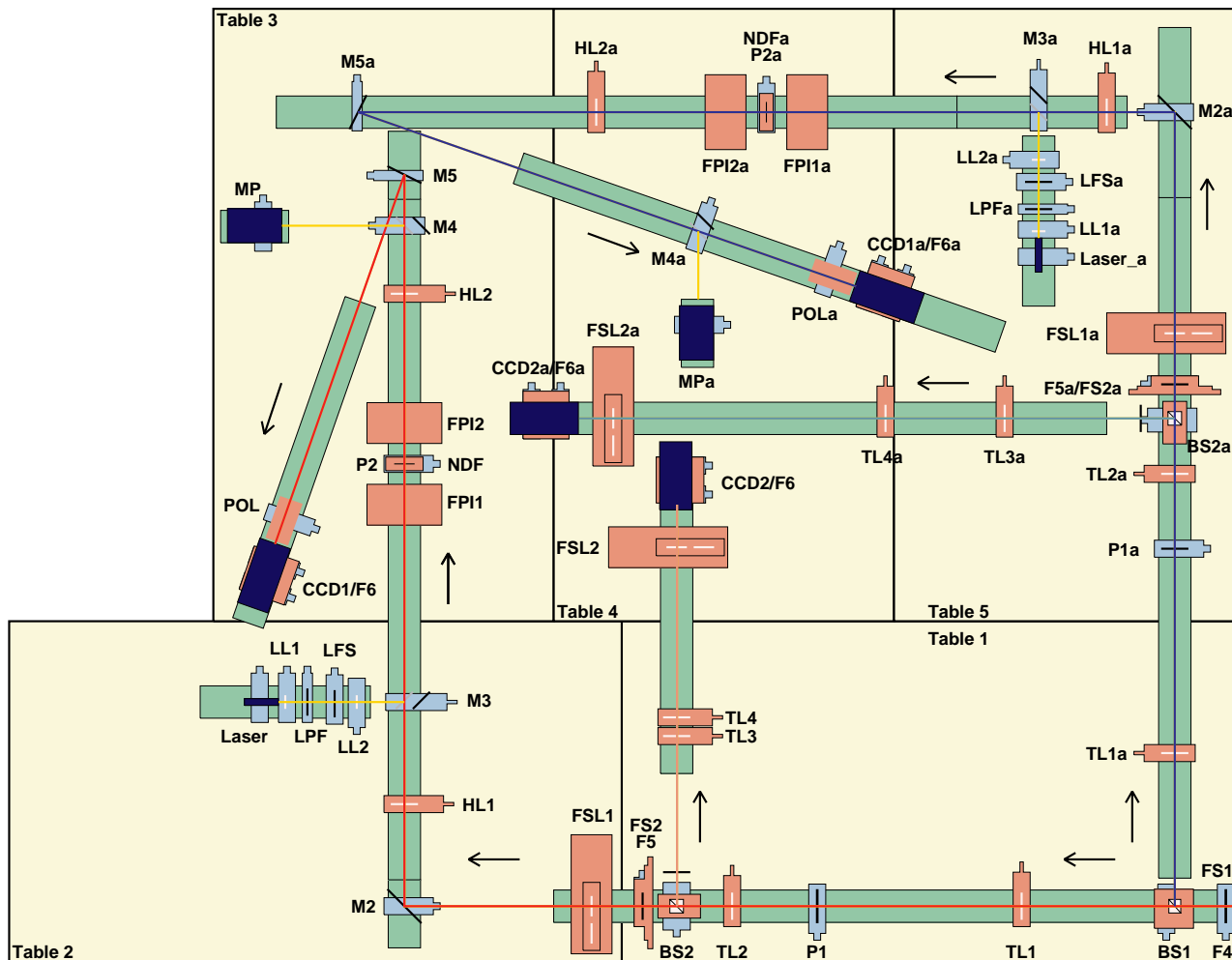


**Fig. 7** Up-to-scale drawing for the integration of BLISS into the GFPI system. The design is based on the study presented in Fig. 8. The optical elements of BLISS are labeled with an extra 'a'. Apart from TL2a, HL2a, and TL4a, they are identical to those of the GFPI. The NBC of GFPI and BLISS is denoted by a red and blue beam, respectively. For the BBC of both instruments, a salmon (GFPI) and turquoise (BLISS) beam distinguish between the two instruments. Laser/Photomultiplier channels of both instruments are highlighted by a yellow beam. The light from the telescope enters at the science focus F4. Black arrows denote the light direction inside both instruments.

cadence of the observations is high enough to trace nearly continuously the temporal evolution.

The restored broad- and narrow-band images presented here have been obtained by a speckle reconstruction<sup>42,43</sup> of the broad-band raw data and a subsequent speckle deconvolution<sup>45,44</sup> of the narrow-band raw data. In the case of time series, the temporal evolution of line parameters in 2D-maps has been obtained after additional data reduction, e.g., image de-rotation/correlation and sub-sonic filtering.<sup>23</sup> In summary, these first observations with the GFPI and GAOS are very promising and suggest that high-cadence 2D spectroscopic observations near the diffraction limit are very likely to be obtained in coming observing campaigns at GREGOR.

### 5 Blue Imaging Solar Spectrometer

The spatial resolution of a telescope scales inversely proportional with the observed wavelength. Therefore, observations at short wavelengths (below 530 nm) offer the oppor-

tunity to obtain data with higher spatial resolution. There are relatively few ground-based instruments for spectral observations in the blue spectral region.<sup>46,47,48,49</sup> All of these observations were carried out with slit-spectrographs that permit only limited improvements by post-factum restoration techniques,<sup>32</sup> which are however applicable to Fabry-Pérot-based imaging spectrometers. This motivated the design of BLISS, which will supplant the blue imaging channel of the GFPI in the near future.

#### 5.1 Spectral lines in the blue part of the visible spectrum

In the wavelength range covered by BLISS, there are several spectral lines and two molecular bands (G-band  $\lambda 430$  nm and CN band-head  $\lambda 388$  nm) of high scientific interest. All Balmer-lines except  $H\alpha$  are at shorter wavelengths than 530 nm, and the Ca II H and K lines are the strongest lines in the visible part of the solar spectrum probing the chromosphere. Several photospheric resonance lines such as Mg I

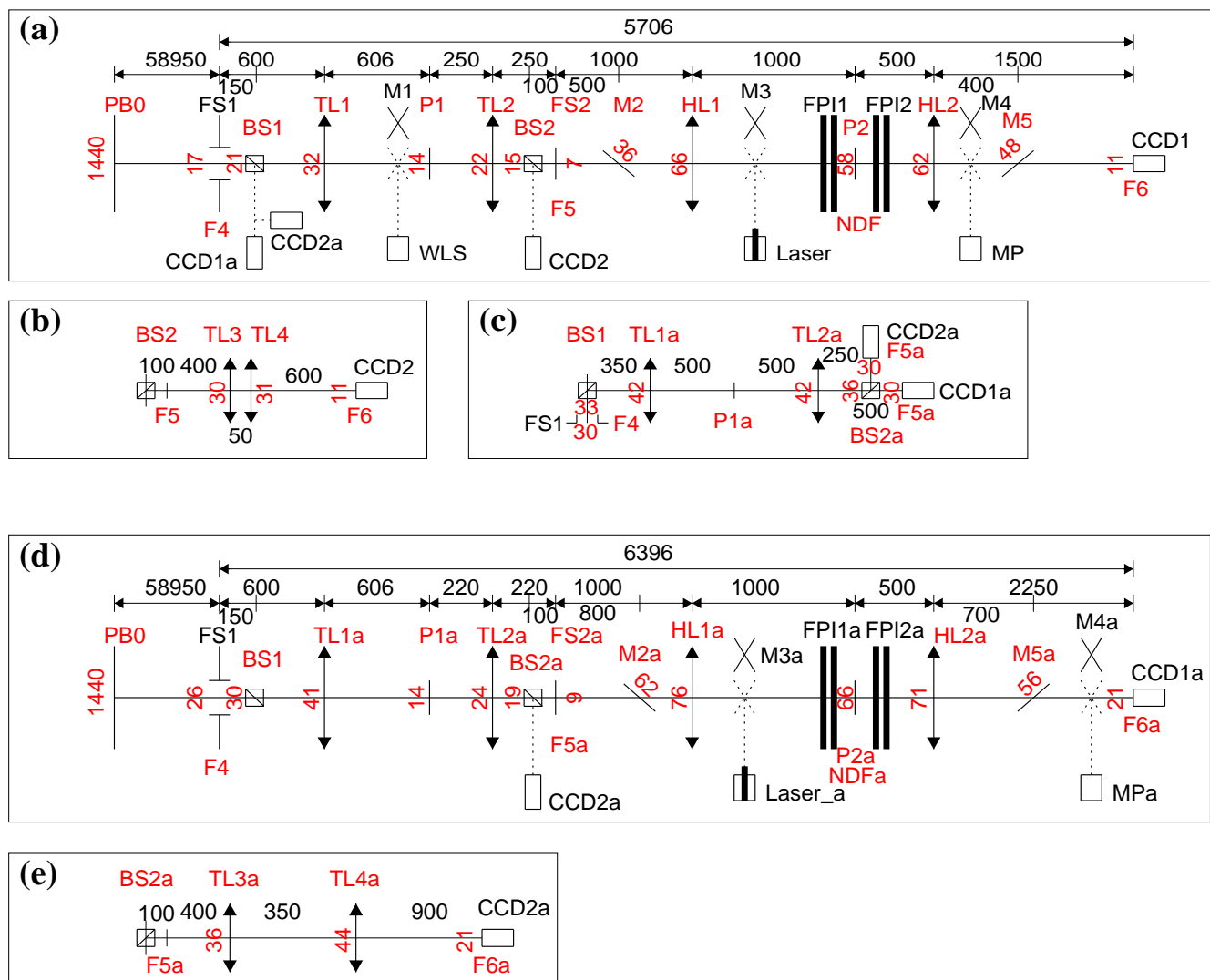


**Fig. 8** Schematic optical design of the current GFPI narrow-band channel NBC (a), broad-band channel BBC (b), and blue imaging channel BIC (c). In the future, NBC (d) and BBC (e) of BLISS will replace the BIC of the GFPI. The diameter of the beam at all optical surfaces, the focal length of the lenses, and the positions of other optical elements are given in millimeters. The optical elements of BIC and BLISS are labeled with an extra 'a'. The achromatic lenses TL2a, HL2a, and TL4a of BLISS have a focal length of 220 mm, 2250 mm, and 900 mm, respectively. The mirrors M2 and M5 of the GFPI will be moved for the integration of BLISS by 200 mm and 50 mm, respectively.

$\lambda 457$  nm, Sr II  $\lambda 407$  nm, and Ba II  $\lambda 455$  nm are found in blue part of the visible spectrum, which also contains several magnetically insensitive lines<sup>50</sup> with  $g_{\text{eff}} = 0$  and lines exhibiting a Zeeman-triplet with splitting factors of  $g_{\text{eff}} = 2.5$  and higher.<sup>51</sup> A special case is the pair Fe I  $\lambda 461.32$  nm ( $g_{\text{eff}} = 0$ ) and Cr I  $\lambda 461.37$  nm ( $g_{\text{eff}} = 2.5$ ) that can be recorded at the same time.

## 5.2 Optical design

The geometrical design of BLISS and its integration into the GFPI is depicted in Fig. 7. Most of the optical components and their labels are identical to those in Fig. 1. The calculations for this initial optical design revealed that a pupil P2 of about 70 mm diameter will be sufficient for an acceptable maximal blue-shift over the entire wavelength range at a given image scale and FOV. Thus, the design of BLISS

only requires different camera lenses HL2a and TL4a in the NBC and BBC to obtain an adequate image scale. The reduction of the diameter of P2, caused by several modifications of the telescope since 2007, is compensated in the design of BLISS. The schematic optical designs of both instruments are compared in Fig. 8. The diameter of the light beam at the different foci, pupils, and on the relevant optical surfaces has been calculated by means of geometrical optics and confirmed by a ZEMAX ray-tracing as for the GFPI.<sup>15</sup> The ZEMAX ray-tracing is presented in Fig. 9.

A new type of cameras has been envisaged for BLISS, namely, two sCMOS-cameras from PCO (pco.edge). These cameras have  $2560 \times 2160$  pixels with a pixel size of  $6.5 \mu\text{m} \times 6.5 \mu\text{m}$  similar to the GFPI Imager QE cameras. Using a focal length of  $f = 2250$  mm for HL2 and  $f = 900$  mm for TL4 yields an image scale of  $0.028'' \text{ pixel}^{-1}$  and a FOV

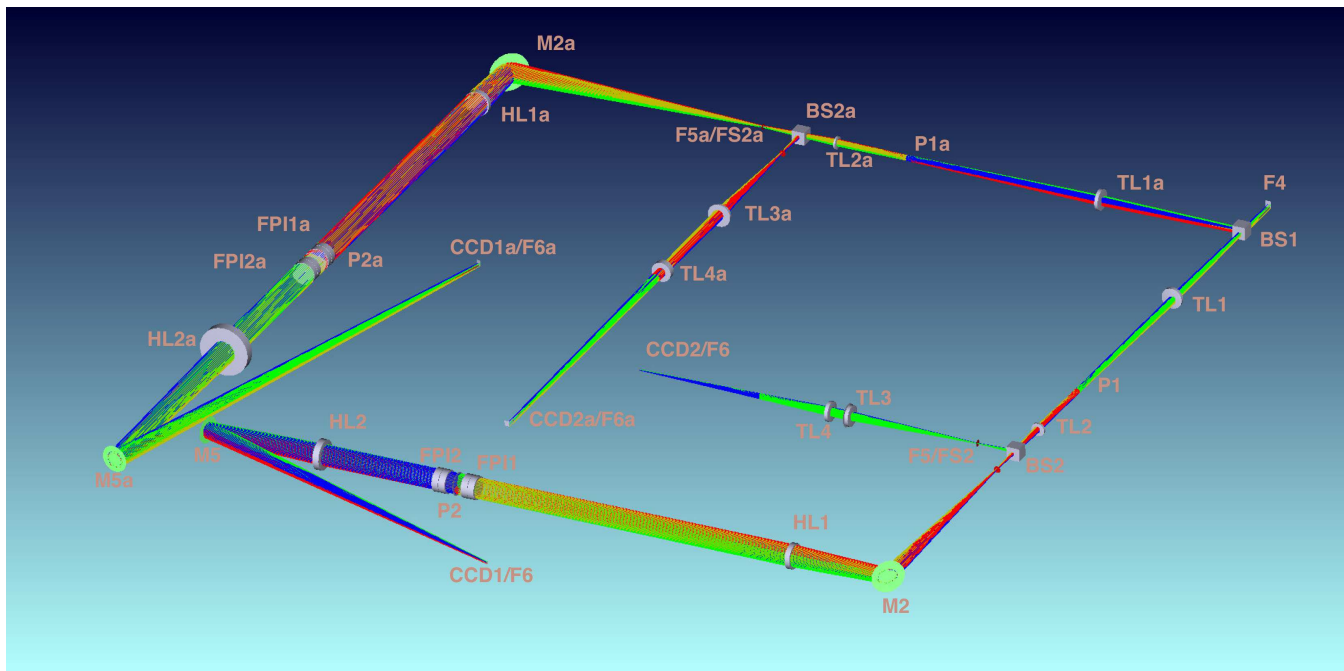


**Fig. 9** Arrangement of GFPI and BLISS in a ZEMAX multi-configuration file in shaded modeling for the respective central wave length of each instrument and their maximal field dimension. The design confirms the calculations in geometrical optics presented in Figs. 7 and 8. The optical elements of BLISS are labeled with an extra 'a'. The light coming from the telescope enters at the science focus F4.

of  $71'' \times 60''$  on both cameras. With this configuration, the maximal blue-shift across the FOV amounts to 4.4 pm and 6.2 pm at 380 nm and 530 nm, respectively.

In addition, we checked the possibility of interchanging the sCMOS and Imager QE cameras between the GFPI and BLISS. The almost identical pixel sizes of both cameras facilitates this task. For the integration of the sCMOS cameras into the GFPI, a circular FOV with a diameter of  $d = 79''$  and an image scale of  $0.036'' \text{ pixel}^{-1}$  for spectroscopy would result in a maximal blueshift of 6.9 pm at 630 nm. However, the FOV for polarimetry is limited by the full-Stokes polarimeter and would remain at its previous size of  $25'' \times 38''$  unless an upgrade of the polarimeter will be undertaken in addition (see Section 3.3). The frame rate at full resolution would increase from 7 to 40 Hz, which perfectly suits this observing mode.

The integration of the Imager QE cameras into BLISS would result in an image scale of  $0.027'' \text{ pixel}^{-1}$  and a FOV of  $38'' \times 29''$  with a maximum blueshift of 1.1 pm and 1.6 pm at 380 nm and 530 nm, respectively. The lower frame rates would match the longer exposure times at shorter wavelength. A super-achromatic optical setup for BLISS – as also foreseen for the GFPI – would be preferable but otherwise all lenses except TL4a of BLISS could be purchased as off-the-shelf achromats.

The distribution of the two instruments on the five optical tables in the GREGOR observing room is shown in Fig. 7. All optical elements of BLISS have been labeled with an additional “a” to distinguish them from those of the GFPI. Behind the common dichroic beamsplitter cube BS1, each instrument has its own NBC and BBC. A displacement of the folding mirrors M2 and M5 of the GFPI to a distance of 700 mm and 350 mm from F5 and HL2, respectively, yields

some free space on optical table 3 that can be used for the NBC of BLISS. The ZEMAX ray-tracing revealed changes in the optical path when considering the etalons plates in the design. Thus, the GFPI NBC has to be shortened further by reducing the distance between P2 and HL2 from 500 mm to 350 mm. This detail is not considered in Figs. 7 and 8.

The beam in the NBC of BLISS is also folded twice by M2a and M5a at a distance of 800 mm and 700 mm from F5a and HL2a, respectively. In the BBC of BLISS, TL3a and TL4a are separated by 350 mm, in contrast to the 50 mm between TL3 and TL4 in case of the GFPI. Two computer-controlled filter sliders FSL1a and FSL2a will again switch between two sets of interference filters. BLISS is mainly designed for spectroscopy because of the expected low photon numbers in the blue spectral region. Nevertheless, a full-Stokes polarimeter can easily be integrated into the system. As in case of the GFPI, a laser/photo-multiplier channel for finesse adjustment of the etalons will be implemented. The white-light channel of the GFPI will be removed and be replaced by an external white-light source shared by all post-focus instruments.

### 5.3 Camera system

Modern sCMOS cameras are capable of delivering high frame rates using large-format sensors with low readout noise, which makes them ideally suited for an application in solar physics. The pco.edge is a potential candidate for BLISS. The camera has a full well capacity of  $30,000 e^-$  and uses 16-bit digitization. The camera has a maximum frame rate of 40 Hz when operated in the global shutter mode. The cameras are running in a “fast scan mode” (286 MHz) converting the 16-bit signal internally to 12-bit because of speed

limitations of the camera link interface. The signal losses due to the compression are roughly a factor of ten smaller than the shot noise of the camera signal. The readout noise is in the order of  $2.3 e^-$ . The dark current consists of a part related to the exposure time, i.e.,  $2\text{--}6 e^- \text{ pixel}^{-1} \text{ s}^{-1}$  and a part related to the sensor readout time, which is constant for a given pixel clock, i.e.,  $0.6 e^- \text{ pixel}^{-1}$ . Peltier cooling of the sensor ensures an operating temperature of  $+5^\circ \text{C}$ . The camera has a quantum efficiency of  $\sim 30\%$  and  $\sim 54\%$  at 380 nm and 530 nm, respectively, similar to the Imager QE cameras currently used in the GFPI ( $\sim 36\%$  and  $\sim 60\%$ ).

To handle the extremely large data acquisition rate of about  $300 \text{ MB s}^{-1}$  at frame rates of 40 Hz, each camera will be controlled by a separate PC, in which the data will be stored on local RAID 0 systems. The integration of the cameras in the control software is straightforward because the DaVis software will be operational on the new system with minor changes only. We will perform first in-situ test-measurements with these cameras during an upcoming GFPI-technical campaign in April 2013 at the GREGOR telescope, whose results will undergo subsequently a careful and detailed analysis.

However, the feasibility of using the pco.edge for BLISS has still to be demonstrated. A detailed evaluation of the photon statistic in the wavelength range 380–530 nm will help with the final decision. Rather long exposure times can be expected for the blue wavelength range and the exposure time of the cameras currently has an upper limit of 100 ms due to a relatively high dark current in the global shutter mode. On the other hand, high frame rates would be extremely beneficial when operating the GFPI in the vector polarimetric mode, because at present this instrument is limited to just 5–7 Hz at full resolution. The almost identical pixel size facilitates interchanging the cameras between the two instruments.

#### 5.4 Etalons

The design of a dual-etalon system requires the consideration of several etalon parameters, i.e., absorption, reflectivity, and resulting peak transmission and finesse of both etalons, as well as the correct plate-spacing in order to obtain the appropriate spectral resolution for a given wavelength range together with a low parasitic-light fraction. The latter is defined as the ratio of the intensity transmitted out-of-band to that of the central transmission peak of the resulting Airy-function of the instrument and depends also on the used pre-filter.<sup>23</sup> The reflectivity of etalons for imaging in the blue spectral region has to be lower to increase the FWHM and to accommodate the smaller number of available photons. Therefore, the rejection of parasitic light further away from the central wavelength  $\lambda_0$  becomes more important and narrower interference filters are required. Interference filters with a FWHM of 0.3–0.8 nm provide a good compromise between parasitic light, transmission, and signal-to-noise. Figure 10 shows the results of such a parameter study for BLISS together with the results obtained for the current etalon properties of the GFPI. In both panels, the transmission profiles of the individual etalons and the order-sorting interference filters (FWHM = 0.3 nm, 40% transmission) are presented for center wavelengths of 600 nm (GFPI, upper panel) and 400 nm (BLISS, lower panel), respectively.

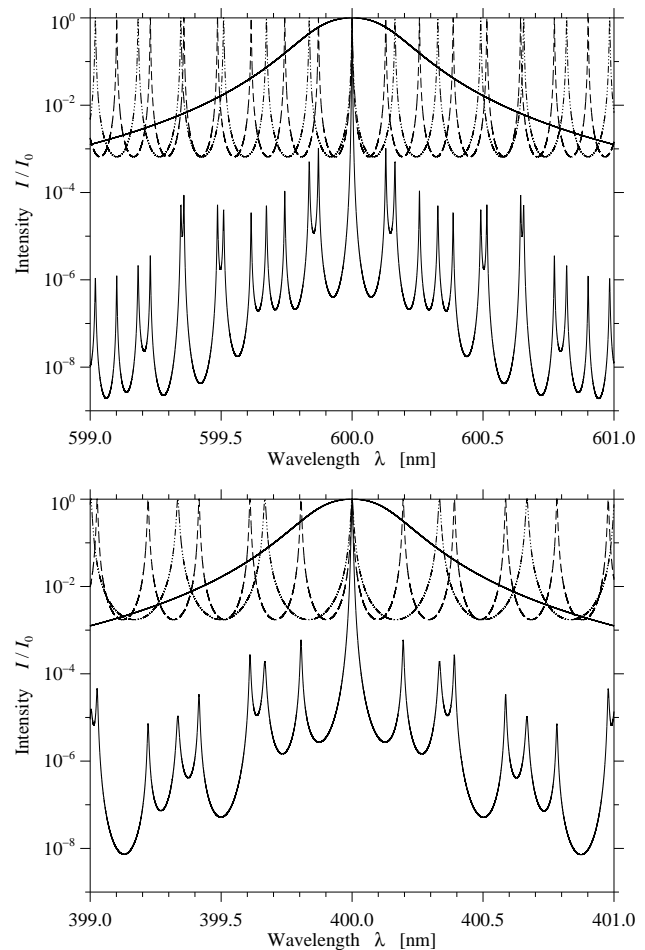


**Fig. 10** Comparison of GFPI (top) and BLISS (bottom) transmission profiles. The curves correspond to a narrow-band interference filter (FWHM = 0.3 nm, thin solid line), etalon 1 ( $R = 0.95/0.92$ ,  $d = 1.4/0.41$  mm, FWHM = 2.1/5.2 pm, thin dashed line), etalon 2 ( $R = 0.95/0.92$ ,  $d = 1.1/0.24$  mm, FWHM = 2.7/8.9 pm, thin dash-dotted line), and all transmission curves combined (FWHM = 1.5/4.2 pm, parasitic-light fraction 0.8/0.4%, thick solid line). The transmission profiles are normalized to unity at the central wavelength  $\lambda_0 = 600.0/400.0$  nm.

The final BLISS and GFPI transmission profiles (thin solid curve) are multiplied by the transmission curve of the pre-filters (thick solid curve) and have a central peak with a FWHM of 1.5 pm and 4.2 pm, respectively. The parasitic-light fraction has been calculated according to the wavelength range of the assumed pre-filter, i.e.,  $\pm 3.5$  nm, and amounts to 0.8% and 0.4% for GFPI and BLISS, respectively. The lower parasitic-light fraction of BLISS is a direct result of optimizing the ratio of the plate spacings which could be done only partly in case of the GFPI.<sup>23</sup> In principle, a larger parasitic light fraction should be expected in the blue. Our results also show that only 0.3 nm interference filters will work with BLISS. In contrast to the GFPI etalons with plate spacings of  $d = 1.1$  and 1.4 mm (FWHM = 2.7 and 2.1 pm) and reflectivities of 95%, for BLISS the combination of etalons with narrower plate spacings of  $d = 0.24$  and 0.41 mm (FWHM = 8.9 and 5.2 pm) and lower reflectivities of 92% will increase the light level and result in a theoretical spectral resolution of  $\mathcal{R} \sim 100,000$ . A proper



wavelength-dependent parameter study like in the case of the GFPI<sup>23</sup> requires the knowledge of the etalon characteristics provided by the manufacturer, thus the present calculations should be extended as soon as this information is available.

## 6 Summary and conclusion

Much effort has been spent to provide with the GFPI a modern first-light post-focus instrument for the GREGOR solar telescope. New software and hardware provide now an easy handling of the instrument with automated procedures for both observation and calibration. The GFPI can be controlled with a well-structured Graphical User Interface (GUI) and underwent an extended commissioning in 2011 and a careful science verification throughout 2012. The latter revealed that most of the characteristic parameters of the instrument comply with the theoretical expectations. However, we are aware of a problem concerning the measured effective spectral resolution of the instrument, which warrants further investigation.

The results from first 2D spectroscopic observations supported by adaptive optics at the end of July 2012 are very promising and suggest that high-cadence 2D spectroscopic observations near the diffraction limit are very likely to be obtained in coming observing campaigns at the GREGOR telescope as soon as the apparent stray-light problem is solved. This will also increase significantly the performance of the adaptive optics system and will finally permit a resolution of about 50 km on the solar surface in combination with post-factum image restoration techniques. Vectorpolarimetric observations will follow in the first half of 2013.

Possibilities for the extension of polarimetric observations to the entire wavelength range covered by the instrument (530–860 nm) are under investigation. We also discussed a future upgrade with new cameras, which would both yield higher frame rates and a larger field-of-view. This would be crucial especially for the dual-beam spectropolarimetric mode of the GFPI, although the enlargement of the field-of-view would require also a re-design of the polarimeter.

The future combination of the GFPI with its companion, the BLue Imaging Solar Spectrometer (BLISS), whose design was presented here in detail, and the GRIS will permit multi-wavelength observations over the entire optical spectral range 380–1600 nm. This will allow one to study the connection of different physical processes from the lowermost photosphere, i.e., the continuum forming layers, up to the upper chromosphere, e.g., the line core of H $\alpha$ , at highest spatial resolution in unprecedented intrinsic detail.

## Acknowledgments

The 1.5-meter GREGOR solar telescope was built by a German consortium under the leadership of the Kiepenheuer-Institut für Sonnenphysik in Freiburg with the Leibniz-Institut für Astrophysik Potsdam, the Institut für Astrophysik Göttingen, and the Max-Planck-Institut für Sonnensystemforschung in Katlenburg-Lindau as partners, and with contributions by the Instituto de Astrofísica de Canarias and the Astronomical Institute of the Academy of Sciences of the Czech Republic. CD was supported by grant DE 787/3-1 of the Deutsche Forschungsgemeinschaft (DFG). We would like to thank Robert Geissler for his competent and extended

help during the science verification.

## References

- Scharmer, G. B., Bjelksjö, K., Korhonen, T. K., Lindberg, B., and Pettersson, B., "The 1-meter Swedish solar telescope", *Proc. SPIE* **4853**, 341 (2003).
- Kosugi, T., Matsuzaki, K., Sakao, T., Shimizu, T., Sone, Y., Tachikawa, S., et al., "The Hinode (Solar-B) mission: an overview," *Sol. Phys.* **243**, 3 (2007).
- Solanki, S. K., Barthol, P., Danilovic, S., Feller, A., Gandorfer, A., Hirzberger, J., et al., "SUNRISE: instrument, mission, data, and first results", *ApJL* **723**, L127 (2010).
- Schmidt, W., von der Lühe, O., Volkmer, R., Denker, C., Solanki, S., Balthasar, H., et al., "The GREGOR solar telescope on Tenerife", *ASP Conf. Ser.* **463**, 365 (2012).
- Schmidt, W., von der Lühe, O., Volkmer, R., Denker, C., Solanki, S., Balthasar, H., et al., "The 1.5 meter solar telescope GREGOR", *AN* **333**, 796 (2012).
- Denker, C., Goode, P. R., Ren, D., Saadehvaziri, M. A., Verdoni, A. P., Wang, H., et al., "Progress on the 1.6-meter New Solar Telescope at Big Bear Solar Observatory", *Proc. SPIE* **6267**, 62670A (2006).
- Cao, W., Gorceix, N., Coulter, R., Coulter, A., and Goode, P. R., "First light of the 1.6 meter off-axis New Solar Telescope at Big Bear Solar Observatory", *Proc. SPIE* **7733**, 773330 (2010).
- Wagner, J., Rimmele, T. R., Keil, S., Hubbard, R., Hansen, E., Phelps, L., et al., "Advanced Technology Solar Telescope: a progress report", *Proc. SPIE* **7012**, 701201 (2008).
- Collados, M., Bettonvil, F., Cavaller, L., Ermolli, I., Gelly, B., Grivel-Gelly, C., et al., "European Solar Telescope: project status", *Proc. SPIE* **7733**, 77330H (2010).
- Puschmann, K. G. and Beck, C., "Application of speckle and (multi-object) multi-frame blind deconvolution techniques on imaging and imaging spectropolarimetric data", *A&A* **533**, A21 (2011).
- Martínez Pillet, V., Del Toro Iniesta, J. C., Álvarez-Herrero, A., Domingo, V., Bonet, J. A., González Fernández, L., et al., "The Imaging Magnetograph eXperiment (IMaX) for the Sunrise balloon-borne solar observatory," *Sol. Phys.* **268**, 57 (2011).
- Rimmele, T. R., Wagner, J., Keil, S., Elmore, D., Hubbard, R., Hansen, E., et al., "The Advanced Technology Solar Telescope: beginning construction of the world's largest solar telescope", *Proc. SPIE* **7733**, 77330G (2010).
- Bendlin, C., Volkmer, R., and Kneer, F., "A new instrument for high resolution, two-dimensional solar spectroscopy," *A&A* **257**, 817 (1992).
- Puschmann, K. G., Kneer, F., Seelemann, T., and Wittmann, A. D., "The new Göttingen Fabry-Pérot spectrometer for two-dimensional observations of the Sun," *A&A* **451**, 1151 (2006).
- Puschmann, K. G., Kneer, F., Nicklas, H., and Wittmann, A. D., "From the "Göttingen" Fabry-Pérot interferometer to the GREGOR FPI", 2007masfa.conf, 45 (2007).
- Bello González, N. and Kneer, F., "Narrow-band full Stokes polarimetry of small structures on the Sun with speckle methods," *A&A* **480**, 265 (2008).
- Balthasar, H., Bello González, N., Collados, M., Denker, C., Hofmann, A., Kneer, F., and Puschmann, K. G., "A full-Stokes polarimeter for the GREGOR Fabry-Pérot interferometer", *IAU Symp.* **259**, 665 (2009).
- Balthasar, H., Bello González, N., Collados, M., Denker, C., Feller, A., Hofmann, A., et al., "Polarimetry with GREGOR," *ASP Conf. Ser.* **437**, 351 (2011).
- Denker, C., Balthasar, H., Hofmann, A., Bello González, N., and Volkmer, R., "The GREGOR Fabry-Pérot interferometer: a new instrument for high-resolution solar observations", *Proc. SPIE* **7735**, 77356M (2010).
- Halbgewachs, C., Caligari, P., Glogowski, K., Heidecke, F., Knobloch, M., Mustedanagic, M., et al., "Telescope Control System," *AN* **333**, 840 (2012).
- Puschmann, K. G., Balthasar, H., Bauer, S. M., Hahn, T., Popow, E., Seelemann, T., et al., "The GREGOR Fabry-Pérot Interferometer – a new instrument for high-resolution spectropolarimetric solar observations", *ASP Conf. Ser.* **463**, 423 (2012).
- Puschmann, K. G., Balthasar, H., Beck, C., Louis, R. E., Popow, E., Seelemann, T., et al., "The GREGOR Fabry-Pérot Interferometer –

- status report and prospects”, *Proc. SPIE* **8446**, 844679 (2012).
23. Puschmann, K. G., Denker, C., Kneer, F., Al Erdogan, N., Balthasar, H., Beck, C., et al., “The GREGOR Fabry-Pérot Interferometer”, *AN* **333**, 880 (2012).
  24. Strassmeier, K. G., Ilyin, V., Woche, M., Granzer, T., Weber, M., Weingrill, J., et al., “Gregor@night: the future high-resolution stellar spectrograph for the GREGOR solar telescope”, *AN* **333**, 901 (2012).
  25. Hammerschlag, R.H. Kommers, J. N., Visser, S., Bettonvil, F. C. M., van Schie, S. J. van Leverink, G., “Open-foldable domes with high-tension textile membranes – The GREGOR dome,” *AN* **333**, 830 (2012).
  26. Soltau, D. Volkmer, R. von der Lühe, O and Berkefeld, T., “Optical design of the new solar telescope GREGOR”, *AN* **333**, 847 (2012).
  27. Volkmer, R., Eisenträger, P., Emde, P. Fischer, A. von der Lühe, O., Nicklas, H., et al., “Mechanical design of the solar telescope GREGOR,” *AN* **333**, 816 (2012).
  28. Berkefeld, T., Schmidt, D., Soltau, D., von der Lühe, O., and Heidecke, F., “The GREGOR Adaptive Optics System”, *AN* **333**, 863 (2012).
  29. Hofmann, A., Arlt, K., Balthasar, H., Bauer, S.M., Bittner, W., Paschke, J., et al., “The GREGOR polarimetric calibration unit”, *AN* **333**, 854 (2012).
  30. Collados, M., López, R., Páez, E., Hernández, E., Reyes, E., Calcines, A., et al., “GRIS – The GRating Infrared Spectrograph for GREGOR”, *AN* **333**, 872 (2012).
  31. von der Lühe, O., Volkmer, R., Kentischer, T., and R. Geißler, “The Gregor Broad Band Imager”, *AN* **333**, 894 (2012).
  32. Beck, C., Rezaei, R., and Fabbian, D., “Stray-light contamination and spatial deconvolution of slit-spectrograph observations”, *A&A* **535**, A129 (2011).
  33. Löfdahl, M. G. and Scharmer, G. B., “Sources of straylight in the post-focus imaging instrumentation of the Swedish 1-m Solar Telescope”, *A&A* **537**, A80 (2012).
  34. Kurucz, R. L., Furenlid, I., Brault, J. and Testerman, L., “Solar flux atlas from 296 to 1300 nm”, National Solar Observatory, Sunspot, NM (1984)
  35. Neckel, H., “Announcement: spectral atlas of solar absolute disk-averaged and disk-center intensity from 3290–12510 Å”, *Sol. Phys.* **184**, 421 (1999).
  36. Allende Prieto, C., Asplund, M., and Fabiani Bendicho, P., “Center-to-limb variation of solar line profiles as a test of NLTE line formation calculations”, *A&A* **423**, 1109 (2004).
  37. Cabrera Solana, D., Bellot Rubio, L. R., Beck, C., and Del Toro Iniesta, J. C., “Temporal evolution of the Evershed flow in sunspots. I. Observational characterization of Evershed clouds”, *A&A* **475**, 1067 (2007).
  38. Denker, C. and Tritschler, A., “Measuring and Maintaining the Plate Parallelism of Fabry-Pérot Etalons”, *PASP* **117**, 1435 (2005).
  39. Scharmer, G. B. “Comments on the optimization of high resolution Fabry-Pérot filtergraphs”, *A&A* **447**, 1111 (2006).
  40. Righini, A., Cavallini, F., and Reardon, K. P., “Imaging performance of multi-etalon bidimensional spectrometers”, *A&A* **515**, 7 (2010).
  41. Schnerr, R. S., de La Cruz Rodríguez, J., van Noort, M. S., “Stokes imaging polarimetry using image restoration: a calibration strategy for Fabry-Pérot based instruments”, *A&A* **534**, 45 (2011).
  42. de Boer, C. R., “*Speckle-Interferometrie und ihre Anwendungen auf die Sonnenbeobachtung*”, PhD thesis, Universitäts-Sternwarte Göttingen, Germany (1993).
  43. Puschmann, K. G. and Sailer, M., “Speckle reconstruction of photometric data observed with adaptive optics”, *A&A* **454**, 1011 (2006).
  44. Janssen, K., “Structure and dynamics of small scale magnetic fields in the solar atmosphere Results of high resolution polarimetry and image reconstruction”, PhD Thesis, Georg-August Universität Göttingen, Germany (2003)
  45. Keller, C. U. and von der Lühe, O., “Solar speckle polarimetry”, *A&A* **261**, 321 (1992)
  46. Lites, B. W., Rutten, R. J., and Kalkofen, W., “Dynamics of the solar chromosphere. I - Long-period network oscillations”, *ApJ* **414**, 345 (1993).
  47. Rouppe van der Voort, L. H. M., “Penumbral structure and kinematics from high-spatial-resolution observations of Ca II K”, *A&A* **389**, 1020 (2002).
  48. Beck, C., Schmidt, W., Kentischer, T., and Elmore, D., “Polarimetric Littrow Spectrograph - instrument calibration and first measurements”, *A&A* **437**, 1159 (2005).
  49. Beck, C., Schmidt, W., Rezaei, R., and Rammacher, W., “The signature of chromospheric heating in Ca II H spectra”, *A&A* **479**, 213 (2008).
  50. Sistla, G. and Harvey, J. W., “Fraunhofer lines without Zeeman splitting”, *Sol. Phys.* **12**, 66 (1970).
  51. Harvey, J. W., “Fraunhofer lines with large Zeeman splitting”, *Sol. Phys.* **28**, 9 (1973).



**Klaus G. Puschmann** performed his thesis at the Instituto de Astrofísica de Canarias (IAC) and received his doctoral degree from the Karl-Franzens Universität Graz in 2002. After post-doctoral positions at the Institut für Astrophysik Göttingen and the IAC, he is presently employed at the Leibniz-Institut für Astrophysik Potsdam. His research interests include image reconstruction, spectropolarimetry and Stokes inversion of sunspot spectra. He is member of the GREGOR project with focus on the development of the GREGOR Fabry-Pérot

Interferometer.



**Manfred Woche** obtained his diploma in physics at the Friedrich-Schiller-Universität Jena in 1976. Until 1996 he was employed at the Karl-Schwarzschild-Observatorium Tautenburg with core responsibilities in spectroscopy and instrumentation. From 1996 until 2001 he worked in optical design and astronomical instrumentation for different institutes, especially for the Max-Planck-Institut für extraterrestrische Physik Garching and the Skinakas Observatory Crete. Since 2001 he is responsible for the optical design of astronomical instrumentation at the Leibniz-Institut für Astrophysik Potsdam.



**Carsten Denker** received his doctoral degree from the Georg-August-Universität Göttingen in 1996. At the Leibniz-Institut für Astrophysik Potsdam, he is the head of the Optical Solar Physics Group and the Solar Observatory Einstein Tower. He is teaching astronomy, astrophysics, and solar physics at the Universität Potsdam and the Humboldt-Universität zu Berlin. His main research interests are in the areas of solar physics, instrumentation for high-resolution solar observations, and image restoration.



**Christian Beck** obtained his PhD at the Albert-Ludwigs-Universität Freiburg in 2006. He worked as a post-doctoral researcher at the Instituto de Astrofísica de Canarias from 2006 to 2012 with a research focus on instrumentation, the structure of sunspots, and the solar chromosphere. He recently joined the National Solar Observatory in Sunspot, New Mexico, as an instrument scientist.



**Horst Balthasar** studied physics at the Georg-August-Universität Göttingen where he got his doctoral degree in 1984. After scientific stations at the Instituto de Astrofísica de Canarias, the Universität Göttingen, the Fachhochschule Wiesbaden and the Kiepenheuer Institut für Sonnenphysik Freiburg, he works since 1997 as a scientist at the Leibniz-Institut für Astrophysik Potsdam. His main scientific interest is the investigation of the dynamics and magnetic field in sunspots.



**Thomas Seelemann** studied physics at the Georg-August-Universität Göttingen. For the diploma thesis and doctoral dissertation he worked at the Max-Planck Institut für Strömungsforschung in Göttingen in the field of molecular physics and received his doctoral degree in 1980. Since then, he is employed at LaVision GmbH, where he works on cameras and their integration into dedicated experimental applications.



**Rohan E. Louis** completed his PhD at the Udaipur Solar Observatory, India in 2010. He is currently working as a post-doctoral fellow at the Leibniz-Institut für Astrophysik Potsdam where he is involved in scientific investigations of high-resolution imaging-spectropolarimetric observations from the GREGOR Fabry-Pérot Interferometer. His research interests include sunspot fine structure, photospheric magnetic fields, solar adaptive optics, and Stokes inversion codes.



**Reiner Volkmer** received his doctoral degree in physics from the Georg-August-Universität Göttingen in 1995. After his PhD, he was project manager of the data handling system for IBIS on board of the INTEGRAL satellite at the Universität Tübingen. Later on, he was manager of the GREGOR project and is now leading the development of the image stabilization system for the PHI instrument on board the Solar Orbiter.



**Emil Popow** studied physics at the Friedrich-Schiller-Universität Jena and the Humboldt-Universität zu Berlin. He is employee of the Leibniz-Institut für Astrophysik Potsdam, where he worked on the development of scientific instruments and astronomical instrumentation. In 2003, he became the head of AIP's technical division.